Assessment of the partially stirred reactor model for LES in a swirl-stabilized turbulent premixed flame

Fredherico Rodrigues[a,b], José M. García-Oliver[b], José M. Pastor[b], Daniel Mira[a,*]

[a] Barcelona Supercomputing Center (BSC), Plaza Eusebi Güell, Barcelona, 1–3 08034, Spain
[b]CMT – Clean Mobility & Thermofluids, Universitat Politècnica de València, Camino de Vera 46022 Valencia, Spain

Abstract

This study presents an assessment of the Partially Stirred Reactor (PaSR) as a subgrid model for large eddy simulations (LES) of turbulent premixed combustion. The PaSR-LES approach uses a skeletal mechanism for methane/air combustion, and requires the transport of all the species, with a closure for the filtered source terms. The rate of progress for each reaction is given by the mixing and chemical time scales, which are computed from global flame parameters and a turbulent time scale respectively. This model is applied to a swirled combustor exhibiting a V-flame shape attached to the nozzle, subjected to heat loss. LES are carried out for two distinct equivalence ratios at atmospheric pressure. The flow fields and the thermochemical states from PaSR-LES are compared with the experimental data and solutions based on Flamelet Generated Manifolds (FGM). The results show good correlation with the experiments and FGM-LES, though also some sensitivity to the resolution. The approach also reproduces well the effect of heat loss, which is determined by the use of a chemical time scale given by a progress variable. Dedicated analysis of the swirl-stabilized flame on different regions is conducted evaluating the capabilities of the model

*Corresponding author. daniel.mira@bsc.es

to reproduce the burning velocity, flame shape and flame structure.

---

1. Introduction

The accurate description of turbulent combustion is essential for the development of engineering applications like gas turbines or aeronautical engines. Even though combustion science has advanced considerably over the last decades, such applications remain challenging due to the complex coupled phenomena and the multiphysics nature of the combustion process. Combustion involves complex interactions such as the highly non-linear behaviour of chemical kinetics, he formation of instabilities or the intricate nature of turbulence-chemistry interactions (TCI). Additionally, the wide range of length and time scales in which turbulent combustion happens require precise and efficient modelling closures and algorithms [1].

Recently, the use of Large Eddy Simulation (LES) has become more popular for the study of turbulent flames. In this approach, large scale phenomena can be solved directly on the numerical domain, while the smallest scales are filtered and the subgrid reaction rate is computed by dedicated closure models, of which two main families exist.Flamelet-based models [2, 3] can solve detailed chemistry by the tabulation of low-dimensional data, mapped by a set of control variables with the use of probability Density Functions (PDF's). These models solve for a reduced number of transport equations and have low computational cost. On the other hand, their accuracy and applicability are often limited to specific burning regimes. Finite rate chemistry models (FRC) on the other hand, can be applied more generally to a wide range of conditions, but the large number of transport equations increase the computational cost. Given this reason, such models are often used in combination with skeletal mechanisms. Some examples

of FRC models are the Thickened Flame Model - TFM, [4], the Eddy Dissipation Concept - EDC, [5], the Linear-Eddy Model - LEM, [6], the Conditional Moment Closure - CMC, [7], and transported PDF methods. Tabulated models have been widely used for solving turbulent flames, however, with the advancements in High Performance Computing (HPC) and the development of efficient algorithms over the last decade, finite rate models can now be applied to complex LES cases with acceptable computational times [1].

In the context of finite rate modelling, reactor-based models are a particular family in which each cell in the LES domain is treated as a chemical dimensionless reactor. The Partially Stirred Reactor (PaSR) proposed by Vulis et al. [8] separates each cell into a reacting portion called the fine structures and a mixing portion called the surroundings. The filtered reaction rate is then computed as the product of the reaction rate in the fine structures and the volumetric reacting fraction, which is dictated by the mixing and chemical time scales.

Chomiak et al. [9] used the PaSR to study diesel sprays in combustion engines, proving that the model could replicate fundamental fluid dynamics and recover experimental lift-off heights. Baudoin et al. [10] carried out a comparison of between PaSR, Level-Set G-Equation [11], TFM, EDC and an analytically Presumed Probability Density Function. The LES was applied to a bluff-body stabilized premixed flame, showing that all models were comparable for recovering flame dynamics and structure. Sabelnikov et al. [12] expanded the base model into the Extended PaSR (EPaSR), where an additional equation is resolved accounting for subgrid convection and diffusion effects, showing improved results on flame structure and dynamics compared to classical PaSR, but at an increased computational cost. Iavarone et al. [13] explored the PaSR model with the use of multiple reacting fractions in Moderate or Intense Low oxygen Dilution (MILD) combustion. Their approach introduced errors in the

total mass balance but resulted in a closer agreement to the experimental NO mass fractions compared to to the use of a global reacting fraction.

An $a\ priori$ study on the definition of the time scales was conducted by Pequin et al. [14] with Direct Numerical Simulation (DNS) data, showing that for a global reacting fraction the choice of the time scale has a major effect. It is found the net chemical production rates that define the Damköhler number can have strong influence on the burning rates. Quadarella et al. [15] explored the use of a modal decomposition of the Jacobian matrix with the goal of using multiple time scales and reacting fractions, showing improvement over the use of global quantities. While these studies were focused mainly on the influence of the chemical time scale, Edwards et al. [16] conducted a Multi-Resolution Analysis (MRA) of the PaSR to optimize the model parameters to reproduce the flow conditions in a methane-hydrogen bluff-body stabilized flame. Three variants of the model [12, 17, 18] were tested to close out the mixing time scale, showing that individual variants were unable to recover the reference data, and combinations of the models were required. Finally, an stochastic analysis of the model was conducted to study ammonia systems by Yu et al. [19], showing how the mixing frequency and radiative heat losses affects temperature and the production of NO_x. Recent publications have shown some applications of the PaSR model for LES in gas turbine conditions. Qian et al. [20] applied the model with different subgrid closures for LES to stratified swirled premixed methane-air flames, being able to capture the effects of stratification and the secondary recirculation zones. Palulli et al. [21] used the model with non-premixed hydrogen flames, being able to identify distinct regions with varying levels of mixing and combustion modes. Recently, Piscopo et al. [22] conducted a sensitivity analysis on the chemical time scale, considering global parameters, showing that not only its definition is critical to achieving stable flames, but also

that the orders of magnitude of mixing and chemical time scales must be similar.

The test case for the present work corresponds to the PRECCINSTA burner by Meier et al. [23], a swirl stabilised atmospheric burner, of which the two stable flames at $\phi = 0.75$ and $\phi = 0.83$ have been extensively investigated. Early LES studies were carried out by Roux et al. [24] with the use of the Thickened Flame model (TFLES) and Galpin et al. [25] with a coupling of tabulated chemistry and presumed PDF's. Both works found a good agreement to the mean velocity fields, as well as for temperature and major species in the latter. Fiorina et al. [26] applied the Filtered Tabulated Chemistry for LES (F-TACLES) model to the burner in perfectly premixed and adiabatic conditions, being able to replicate temperature and CO_2 profiles to a reasonable degree. Wang et al. conducted similar study [27] using the Reaction-Diffusion Manifold (REDIM) method showing good agreement to the experiments. Later on [28], the Dynamically Thickened Flame (DTF) and a Flame Surface Density (FSD) model were also compared with similar results, showing that although both models are similar in general terms, a better description for the CO distribution is found by the DFT model, with the source of this difference pointed to the creation of the chemistry table in the FSD method. Franzelli et al. [29] investigated the perfectly premixed assumption in LES using a two-step mechanism and the DTF model, showing that the assumption is valid for the stable regime at $\phi = 0.83$. The influence of partial premixing was later further explored by Gövert et al. [30] with the use of tabulated chemistry and presumed PDF's, confirming that it has a limited effect for the stable flames. This study also evaluated the effect of heat losses, showing that it is crucial for a proper description of the flame structure, but using a new turbulent combustion model that has not been employed for this flame before.

In the current work, the flame is simulated with the PaSR, considering a

global reacting fraction value for all species in each LES cell. The FGM approach with presumed PDF's using β-functions is also used for comparison. The chemical time scale is computed based on flame parameters similar to the ones used for FGM, while the mixing time scale is calculated based on a subgrid turbulent time scale. The focus is given to evaluate the the predicting capabilities of the model in premixed combustion with heat loss and the influence of mesh resolution on the final results. The modelling approach is presented in Section 2, while the case description and results are given in Sections 3 and 4. Conclusions and directions for future work are detailed in Section 5.

2. Mathematical Model

2.1. The Partially Stirred Reactor Model

Considering turbulent reactive flows at a low Mach number, the governing equations correspond to the conservation of continuity, momentum, energy (often written in terms of enthalpy) and chemical species. Using unity Lewis number, the full set of Favre-filtered equations, in order, is given by Eqs. 1a to 1d:

$$\frac{\partial(\overline{\rho})}{\partial t} + \nabla \cdot (\overline{\rho}\widetilde{\mathbf{u}}) = 0, \tag{1a}$$

$$\frac{\partial(\overline{\rho}\widetilde{\mathbf{u}})}{\partial t} + \nabla \cdot (\overline{\rho}\widetilde{\mathbf{u}} \otimes \widetilde{\mathbf{u}}) = -\nabla \overline{p} + \nabla \cdot \boldsymbol{\tau}(\widetilde{\mathbf{u}}), \tag{1b}$$

$$\frac{\partial(\overline{\rho}\widetilde{h})}{\partial t} + \nabla \cdot (\overline{\rho}\widetilde{\mathbf{u}}\widetilde{h}) = \nabla \cdot \left[\overline{\rho}\left(\widetilde{D}_t + \frac{\nu_t}{Sc_t}\right)\nabla\widetilde{h}\right] \tag{1c}$$

$$\frac{\partial(\overline{\rho}\widetilde{Y}_k)}{\partial t} + \nabla \cdot (\overline{\rho}\widetilde{u}\widetilde{Y}_k) = \nabla \cdot \left[\overline{\rho}\left(\widetilde{D}_t + \frac{\nu_t}{Sc_t}\right)\nabla\widetilde{Y}_k\right] + \overline{\dot{\omega}}_k, \tag{1d}$$

where $\overline{\rho}$ is the density, $\widetilde{\mathbf{u}}$ is the velocity vector, $\overline{p}$ represents the pressure, $\boldsymbol{\tau}(\widetilde{\mathbf{u}})$ is the viscous stress tensor, $\widetilde{h}$ is the enthalpy, $\widetilde{D}_t$ represents the thermal diffusivity,

ν_t is the subgrid kinematic viscosity and Sc_t is the subgrid Schmidt number (equal to 0.7). Of special interest for this work is the equation for the transport of species, Eq. (1d), where the terms $\widetilde{Y}_k$ and $\overline{\dot{\omega}}_k$ represent the mass fraction and the filtered reaction rate for species k, respectively. The viscous tensor in the momentum equation uses the Stoke's assumption and is written as $\boldsymbol{\tau}(\widetilde{\mathbf{u}}) = 2\mu\mathbf{S}^{\mathbf{D}}$, with the stress tensor $\mathbf{S} = \left(\frac{1}{2}(\nabla\widetilde{\mathbf{u}} + (\nabla\widetilde{\mathbf{u}})^T)\right)$ and the deviatoric part $\mathbf{S}^{\mathbf{D}} = \left(\frac{1}{2}(\nabla\widetilde{\mathbf{u}} + (\nabla\widetilde{\mathbf{u}})^T)\right) - \frac{1}{3}(\nabla\cdot\widetilde{\mathbf{u}})\mathbf{I}$, where $\mathbf{I}$ is the identity tensor. The unit Lewis assumption is used to write the diffusivity coefficients as $\widetilde{D}_t = \overline{\lambda}/\overline{c}_p$ with $\overline{\lambda}$ representing the thermal conductivity and $\overline{c}_p$ being the specific heat capacity. A gradient hypothesis is used to close the unresolved scalar fluxes [31]. The system is closed by the equation of state (2):

$$\overline{\rho} = \frac{\overline{p}^{th}\overline{W}}{R\widetilde{T}}, \tag{2}$$

with p^{th} being the thermodynamic pressure, $\overline{W}$ the mean molecular weight, R the universal gas constant and $\widetilde{T}$ the temperature, which is solved by means of the transport of enthalpy using NASA polynomials [32].

Without the proper description of the subgrid contribution to the reaction rate, the filtered reaction term cannot be accurately calculated, leading to significant errors. Several strategies have been proposed for the closure of this term, and over the last decade, reactor-based models have become popular [14, 33]. This family of models assumes that each LES cell can be treated as an ideal reactor. The most trivial assumption for such models is that perfect mixing occurs and the reactor is homogeneous, such that the entirety of the cell volume is occupied by fresh gases and is capable of reacting. Such approach does not take into account imperfect mixing caused by turbulent effects, and as such, high resolution is required and the computational cost increases substantially, like in

the direct numerical simulation (DNS) of turbulent flames. Turbulent chemistry interactions in the subgrid scale of the LES cells are described in PaSR by the cell reacting volume fraction, κ, while the rest of the volume accounts for the reduction in chemical reactivity by the effects of turbulence. While this aspect is represented by a presumed shape PDF in the FGM approach, the reacting volume fraction in the PaSR is given by the factor κ. This quantity is estimated from the subgrid scale quantities taken directly from the LES solution. With such, the filtered reaction rate for the PaSR is then written as:

$$\overline{\dot{\omega}}_k = \kappa \dot{\omega}_k^* + (1-\kappa)\dot{\omega}_k^0, \tag{3}$$

where the superscript * represents the reacting region, named fine structures, while the superscript ^{0} represents the non-reacting part, called surroundings. Reaction can only take place within the fine structures, such that the reaction rate in the surroundings is null. Thus, the filtered reaction rate can be re-written as:

$$\overline{\dot{\omega}}_k = \kappa \dot{\omega}_k^*. \tag{4}$$

From here, one needs to estimate both the volume fraction κ and the reaction rate of the fine structures, $\dot{\omega}_k^*$. Starting with the reaction rate and assuming steady state, a mass balance between fine structures and surroundings can be written according to Eq. 5:

$$\rho\left(Y_k^0 - Y_k^*\right) + \dot{\omega}_k^* \tau^* = 0, \tag{5}$$

with τ^* representing the residence time in the fine structures, to be discussed later. Rearranging the terms, the fine structure reaction rate can be expressed as:

$$\dot{\omega}_k^* = \frac{\rho\left(Y_k^* - Y_k^0\right)}{\tau^*}. \tag{6}$$

The unknown in Eq. 6 is the fine structure mass fraction, Y_k^*, which can be understood as the final chemical state of an ideal constant pressure reactor, starting with initial conditions defined in terms of pressure, temperature and mass fraction (P^0, T^0, Y_k^0). In the LES framework, such initial state is given directly from the filtered pressure, temperature and species mass fraction fields, such that $Y_k^0 \approx \widetilde{Y}_k$. Assuming that no significant changes in pressure occur, a constant pressure reactor can be used to estimate the fine structure mass fractions as:

$$\frac{dY_k^*}{dt} = \frac{\dot{\omega}_k}{\overline{\rho}}. \tag{7}$$

In the PaSR, the description of the TCI reduces to the estimation of the volume fraction κ. Different strategies are found in the literature, either with the use a global reacting fraction value for all species in each cell in the numerical domain, or with a matrix of reacting fraction values $[\kappa_0, \kappa_1, \ldots \quad \kappa_n]$ with n being an arbitrary number usually based on the number of species or groups of species that share similar time scales. The reacting volume fraction is given by

$$\kappa = \frac{\tau_c}{\tau_c + \tau_m}, \tag{8}$$

where τ_c represents the chemical time scale and τ_m represents the mixing time scale. It should be noted that, when $\tau_m << \tau_c$, mixing can be considered infinitely fast. This in turn drives $\kappa \to 1$, the fine structures occupy the entirety of the cell and the reactor transitions from a partially to a perfectly stirred reactor regime. On the other hand, if mixing is slow compared to the chemistry, $\kappa \to 0$ and the reaction zone within the cell is considered infinitely thin. In this case, mixing is insufficient to provide the cell with fresh gases and reactivity decreases.

In this work, global values of reacting fraction κ and chemical time scale τ_c are used, with the term $global$ here referring to chemical space, such that in each cell a single reacting fraction handles the reactions for all species. This choice is based on the assumption that, as with flamelet-based models, the flame can be accurately represented by an evolving progress variable, mapping the transition from fresh to burned gases. In this way, the chemical time can be described in terms of the flame parameters rather than the composition space where slow and fast radicals occur simultaneously. The mixing time scale τ_m is similarly based on the dissipation rate of the turbulent kinetic energy, and the reacting fraction relates to both quantities.

2.2. Estimation of the time scales

The estimation of the chemical time scale τ_c is still an open question that depends on several factors, such as chemical composition, burning regime and chemical mechanism. Pequin et al. [14] conducted an extensive study on the accuracy of different definitions of τ_c applied to $a\ priori$ filtered DNS data of a jet flame. In this present work, a number of formulations proposed from [14] were tested, specifically the Fastest Formation Rate (FFR), Slowest Formation Rate (SFR) and Chomiak's formulations, however in general all three approaches resulted in unstable flames and eventual extinction. Such formulations are presented in Table 1, where N_S and N_D are the total number of species and the number of dormant species, respectively. More recently, Piscopo et al. [22] proposed the use of a a new formulation based on the geometrical mean (GFR) of SFR and FFR, though this new formulation did not show any improvement over SFR, while also failing to produce stable flames whenever the relative difference between mixing and chemical times was significant.

The authors here propose a new formulation for τ_c based on time scale of the flame. Assuming that the overall chemistry can be mapped by a progress variable Y_C, which tracks the evolution of the flame from fresh to burned gases and provides a realistic time scale of the flame. The chemical time scale can be expressed in terms of this progress variable:

$$\tau_c = \frac{Y_c}{|\dot{\omega}_{Y_C}|/\rho}, \tag{9}$$

with Y_c being the mass fraction and $\dot{\omega}_{Y_C}$ the reaction rate of the progress variable. The progress variable itself is given by a linear combination of chemical species, namely CO_2 and CO in this case, leading to:

$$Y_c = Y_{CO_2} + Y_{CO}. \tag{10}$$

This is consistent with the definition of a mixing time scale based on a subgrid turbulent kinetic energy evaluated from the cell length, Δ, and the dissipation rate of the kinetic energy, ϵ^{SGS}, which is computed following [34]. The mixing time scale is finally given by:

$$\tau_m = \left(\frac{\Delta^2}{\epsilon^{SGS}}\right)^{1/3}. \tag{11}$$

Each non dimensional reactor is solved up to a residence time equal to $\tau^* = min(\tau_c, \tau_m, dt_{LES})$, with dt_{LES} being the actual timestep of the LES. As

Table 1: Chemical time scale formulations from [14]

τ_c^{FFR}	$min_{i=1,N_S-N_D}\left(\frac{Y_k}{\lvert\dot{\omega}_k\rvert/\rho}\right)$
τ_c^{SFR}	$max_{i=1,N_S-N_D}\left(\frac{Y_k}{\lvert\dot{\omega}_k\rvert/\rho}\right)$
$\frac{1}{\tau_c^{Ch}}$	$max\left(\frac{-\dot{\omega}_F}{Y_F}, \frac{-\dot{\omega}_O}{Y_O}\right)/\rho$

will be discussed in the Results section, these definitions of the time scales, combined with the use of a global reacting fraction, have shown to provide stable flames which are able to correctly recover the flame dynamics and the flame structure.

2.3. Tabulated Chemistry

For the tabulated cases, a Flamelet Generated Manifold (FGM) approach [3] is used. The manifold is constructed with premixed flamelet solutions for decreasing levels of enthalpy, accounting for heat losses. The table is mapped by the scaled progress variable, $C = (Y_c - Y_c^{min})/(Y_c^{max} - Y_c^{min})$, its variance, $C_{var} = \widetilde{C^2} - \widetilde{C}^2$, and normalized enthalpy, $I = (h_c - h_c^{min})/(h_c^{max} - h_c^{min})$. This is coupled with a presumed Probability Density Functions (β-PDF's) approach. The strategy is similar to the one described in [30]. The definition of the progress variable for the tabulated case is the same as the one used for the definition of the chemical time scale on the PaSR ($Y_c = Y_{CO_2} + Y_{CO}$), so a direct comparison between the approaches can be made.

3. Case Description

3.1. Experimental Setup

Table 2: Simulated operating conditions.

Flame	Air mass flow [g/min]	Fuel mass flow [g/min]	P_{th} [kW]	ϕ_{global} [-]	T^{ad}_{global} [K]
A	734.2	35.9	30.0	0.83	2037
B	734.2	32.3	27.0	0.75	1915

The PRECCINSTA is an atmospheric swirled burner developed at the German Aerospace Center (DLR). Among the different conditions, methane-air at atmospheric temperatures and pressure were considered. Air is injected into a plenum while fuel is injected directly in the swirler by means of an array of small radially-distributed inlets. Table 2 shows the parameters for flames A (at $\phi = 0.83$) and B (at $\phi = 0.75$) reported by Meier et al. [23]. The resulting flames are V-shaped, attached to the nozzle and non-oscillating. Note that despite the fact that fuel is injected in the swirler, and fuel-air mixing takes place across the cone-shaped nozzle, the perfectly premixed assumption is valid for these conditions, as demonstrated by Franzelli et al. [35] and Gövert et al. [30]. The available experimental data consists of Raman measurements for flame A, providing fields for temperature and chemical species, and PIV measurements for flame B, providing fields for velocity, as well as OH-PLIF fields for both cases.

3.2. Numerical Setup

Table 3: Numerical mesh sizes.

Mesh	Number of Elements	Element length in Swirler	Element length in Combustion Chamber
4M	4×10^6	1.0 mm	1.0 mm
14M (Baseline)	14×10^6	1.0 mm	0.6 mm
30M	30×10^6	0.5 mm	0.5 mm

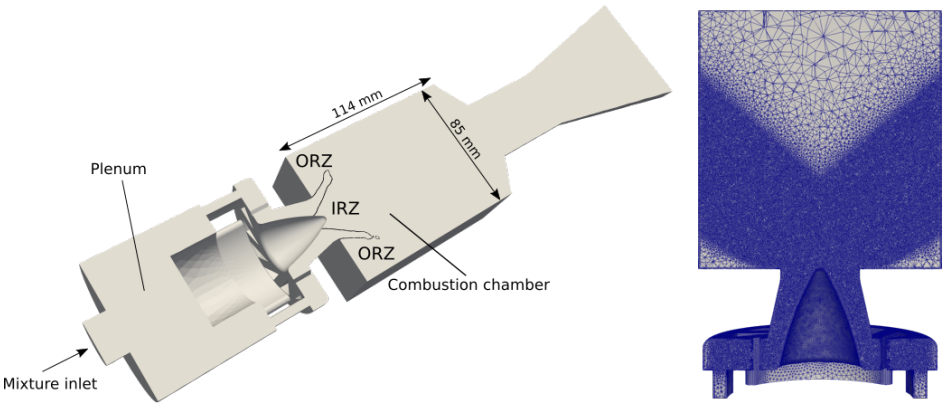

Figure 1: Sketch of half of the numerical domain (left) and mesh refinement on the combustion chamber (right). In the left figure, the plenum, combustion chamber and mixture inlet are shown, with flame position indicated by an iso-contour of progress variable. Also shown are the Inner and Outer Recirculation Zones (IRZ and ORZ respectvely).

For the present work, a numerical domain representing the entire geometry of the PRECCINSTA was constructed. Three distinct versions, with different mesh sizes of four, fourteen and thirty million elements, were used. Figure 1 shows the geometry of the numerical domain (left), with the position of the flame illustrated by a time-averaged iso-contour of progress variable. Also shown is a section of the unstructured 30 million mesh (right), where the refinement on the combustion chamber and swirler can be seen. Naturally, this refinement is centered around the flame region. Table 3 summarizes the meshes with their respective resolutions. These mesh sizes correspond to an unstructured mesh, with the resolution levels shown in Table 4. Simulations with the PaSR are run for the three meshes, while the FGM calculation is conducted on the baseline mesh with 14 million elements.

All simulations are run with the parallel multi-physics code Alya [36] in the context of Large Eddy Simulation (LES). The code uses a low dissipation

numerical scheme based on a continuous Galerkin formulation for low-Mach number flows coupled to scalar transport equations from Both et al. [37], with code vectorization [38] and subgrid model proposed by Vreman et al. [39]. The chemical solver uses a variable order fully implicit scheme - CVODE [40] with a splitting algorithm [41], considering different strategies for chemical integration [42].

The location of the Inner Recirculation Zone (IRZ) and Outer Recirculation Zone (ORZ) are also indicated. A perfectly premixed assumption is considered in this work to focus the analysis on the influence of mesh resolution and heat loss on the predicting capabilities of the model without accounting for the effect of fuel-air mixing. Both tabulated and finite rate cases employ the skeletal chemical mechanism from Luca et al. [43], with 16 and species and 72 reactions. Atmospheric pressure is used, and the fuel-air mixture is injected at an initial temperature of 320 K, following the natural pre-heating reported in the experimental case.

4. Results and Discussion

This section is dedicated to a thorough investigation of the PaSR model for premixed combustion in swirled flames subjected to heat loss. For such, the model needs first to be shown to recover the correct flow dynamics and thermochemical state of the real flame. As previous works have successfully used tabulated chemistry models to replicate both flow dynamics and flame structure [25, 26, 27, 30], the FGM model is used here as a reference numerical solution along with the experimental data. Then, it is possible to compare the two approaches using the same numerics and same mesh resolution to extract additional conclusions. As such, a study of the influence of both mesh resolution and heat losses on

the PaSR quantities is done, showing how the time scales and reacting fraction behaves, with a focus on the reacting layers. Lastly, flame structure itself is analyzed to clarify how well the PaSR can recover the swirled flame when mesh resolution and heat loss effects are accounted for.

4.1. Assessment of model predictions against experimental measurements

The time averaged fields for temperature and velocity are shown in Figure 2 for both FGM and PaSR in the reference mesh for $\phi = 0.75$. The velocity profiles have similar behaviours in the flame front, though small differences can be seen in the position of the inner recirculation zones, with PaSR centering its vortex at a more upstream position. The outer recirculation zones look similar for both cases. The temperature fields are also similar for both models, with PaSR showing a slightly larger flame brush, while also presenting higher temperature in the inner region. Note that the maximum temperature for the FGM case is limited to the flamelet manifold given by the premixed flamelets, while for the PaSR it is computed locally from Arrhenius rates using the filtered quantities with the correction factor κ.

Figure 3 shows the time averaged profiles for the three components of the velocity: axial, radial and tangential. Both the FGM and PaSR models are compared on the reference mesh. Results are compared to experimental PIV data obtained for flame B (equivalence ratio $\phi = 0.75$, thermal power $P_{th} = 27$ kW). The systematic uncertainty for the mean velocity field is about 2.5% [23]. Overall, both models are able to correctly replicate experimental results, with the correct prediction of the position of peaks and troughs, but with small deviations. The axial velocity is shifted to the right in the IRZ for both models from 1.5 mm up to close to 15 mm. Throughout this range, the PaSR agrees

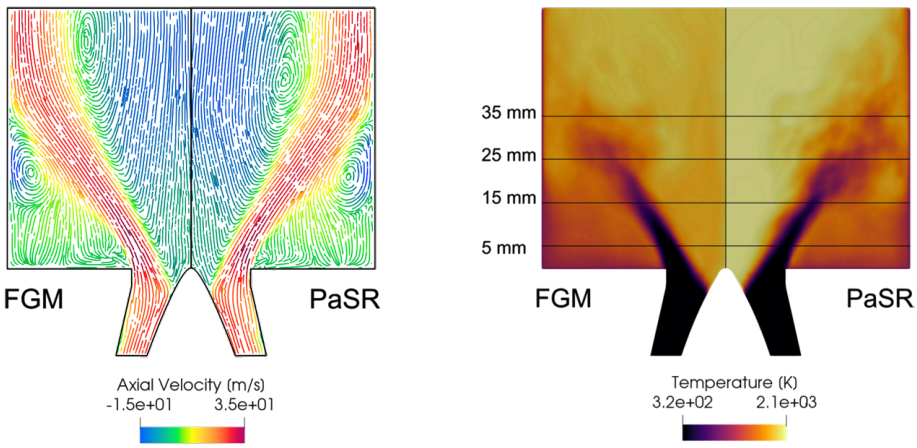

Figure 2: Time-averaged fields for axial velocity and temperature for FGM-14M and PaSR-14M (Flame A).

to the experimental data on the actual flame front and outwards. For the two last downstream positions, axial velocity is slightly underpredicted. The radial velocity is correctly recovered for both models, except in the outer regions of the two most downstream positions, where mesh resolution seems insufficient to capture localized vortexes with strong recirculation. The tangential velocity profiles recover the correct position of peaks as well, and the general behaviour of the experimental data, but also show some deviations, especially in the outer recirculation zone from 1.5 mm to 5 mm.

The Root Mean Square (RMS) velocity profiles are presented in Figure 4. Both models are able to predict the level of fluctuations. In general, peaks are correctly predicted in both location and strength for all the components from 1.5 to 15 mm, although both models underpredict the RMS velocities close to the ORZ. At 25 mm and above, larger deviations appear. It should also be noted that close to the flame region, strong temperature intermittence occurs. For such conditions, Favre (LES) and Reynolds (PIV) averages can differ, which can

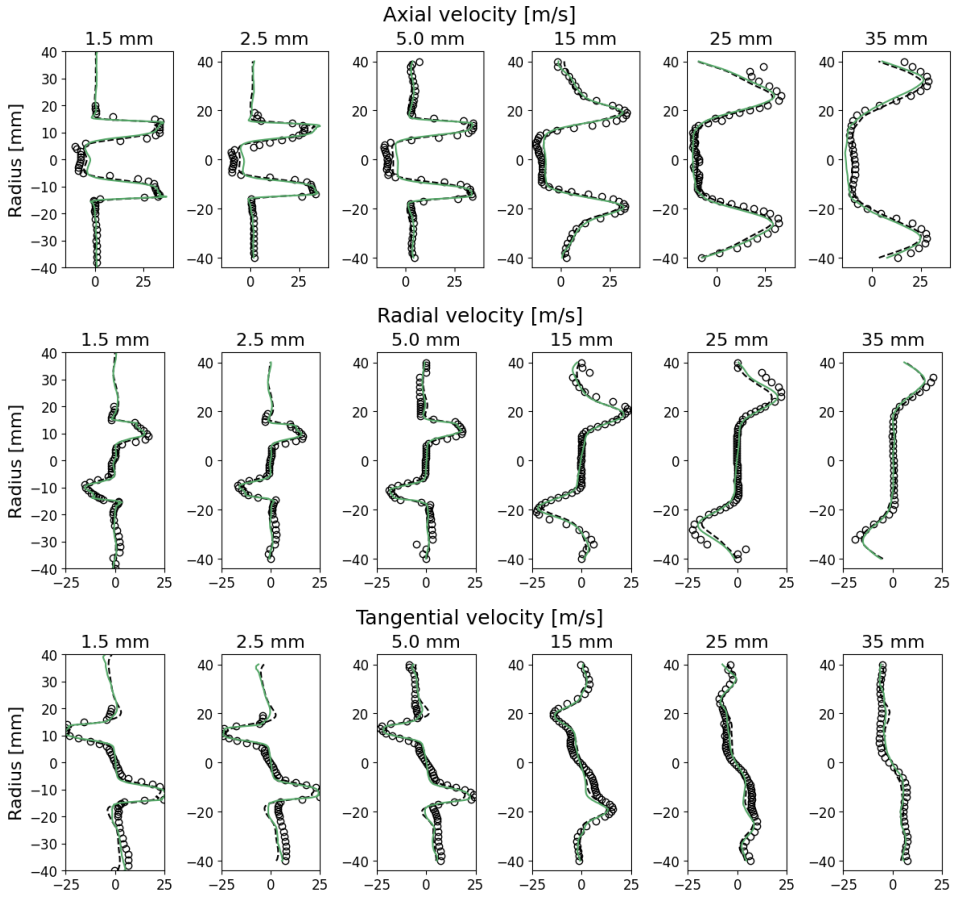

Figure 3: Time averaged velocity profiles (Flame A): Experiments (o), FGM-14M (- ·), PaSR-14M (—)

lead to the apparent deviations seen here [24]. Despite minor deviations at specific regions, the global flow dynamics seem to be accurately replicated by the PaSR at this mesh resolution, recovering the experimental result to a satisfactory degree. Similarly to the mean field, the systematic uncertainty for the RMS measurements is about 3% [23].

Time averaged and RMS temperature profiles are presented in Figure 5 for flame A ($\phi = 0.83$, $P_{th} = 30$ kW). Azimuthal average profiles are obtained

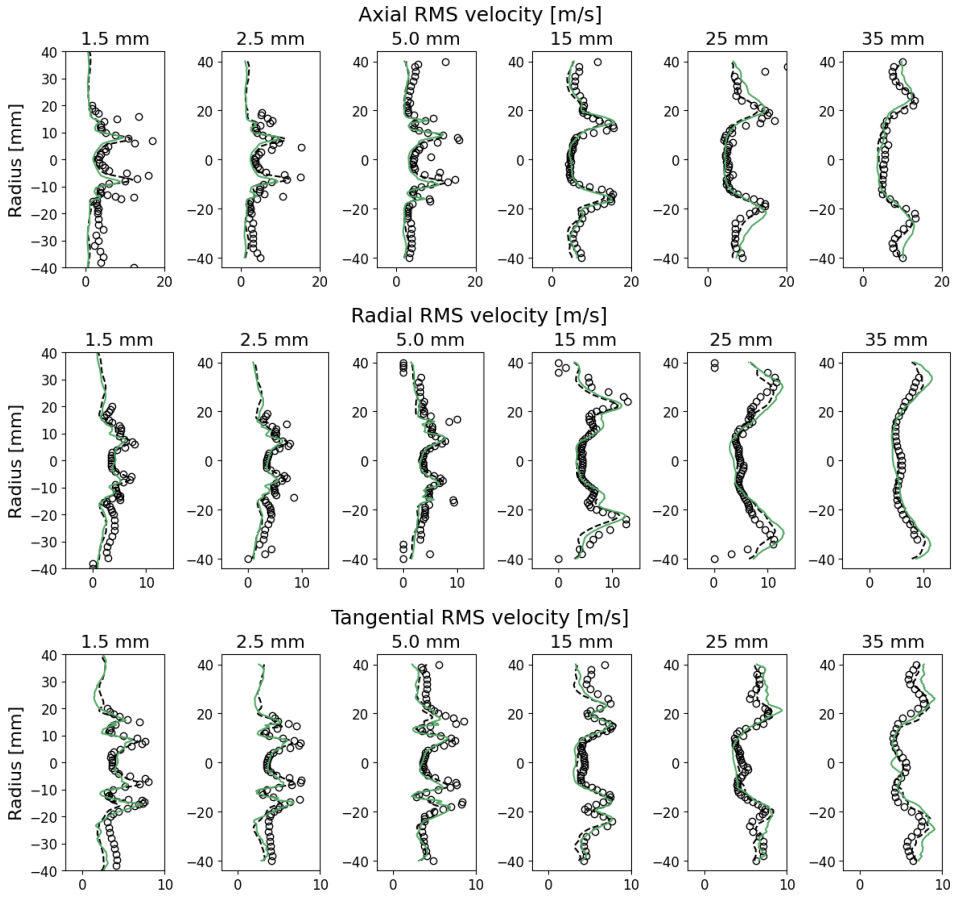

Figure 4: Root Mean Square velocity profiles (Flame A): Experiments (o), FGM-14M (- ·), PaSR-14M (—)

from numerical data, with the dashed black line representing the symmetry axis. PaSR results on the three meshes are compared to both FGM results on the baseline mesh (14M), as well as with the RAMAN data. A dedicated discussion on the effects of mesh resolution will be carried out in the next section. For the mean temperature profiles, the baseline mesh shows consistent results between FGM and PaSR-14M, with PaSR-14M overpredicting temperature in the inner recirculation zone. PaSR-4M shows the highest deviations, overpredicting the

temperature globally. Regarding the shape of the flame, the experimental values are well recovered by the PaSR-30M and provides correct predictions of the temperature distribution at the reacting layers. The position of the inner reacting layer is shifted for FGM-14M and PaSR-14M, and even more so for PaSR-4M, resulting in narrower flame fronts. The maximum instantaneous temperatures for each case are as follows: $T_{adiabatic} = T^{max}_{FGM-14M} = 2037$ K, $T^{max}_{4M} = 2270$ K, $T^{max}_{14M} = 2098$ K and $T^{max}_{30M} = 2079$ K.

Regarding the RMS profiles, all models are able to correctly recover the position of the peaks and troughs. Both PaSR-14 and FGM-14 predict similar peak values at the more upstream positions, but FGM starts to deviate more from the experimental values on the outer region starting at 30 mm. Nevertheless, all the PaSR cases remain close together. Once again, the best agreement is obtained for PaSR-30M, showing the influence of mesh resolution for the PaSR. The reported systematic uncertainty for temperature are of the order of 3-4% [23].

Similarly, Figure 6 shows the time averaged profiles for CO and CO_2 mass fractions. One important caveat is that, even though the systematic uncertainty for species (around 7% for CO_2) is of the same order as the one for temperature (3-4%), it is considerably higher for CO, within the range of 20-50%, with statistical uncertainties also being density dependent [23]. As it will be discussed shortly, the correct prediction of both species is critical for the PaSR, as these are the species used for the computation of the progress variable Y_c and subsequently the chemical time scale τ_c.

The predictions for CO vary greatly for all models. At both 6 and 10 mm, two peaks are present, which correspond the inner and outer reacting layers at each height. All numerical results present higher values compared to the experiments, with PaSR-30M showing the closest overall agreement, while FGM-14M presents

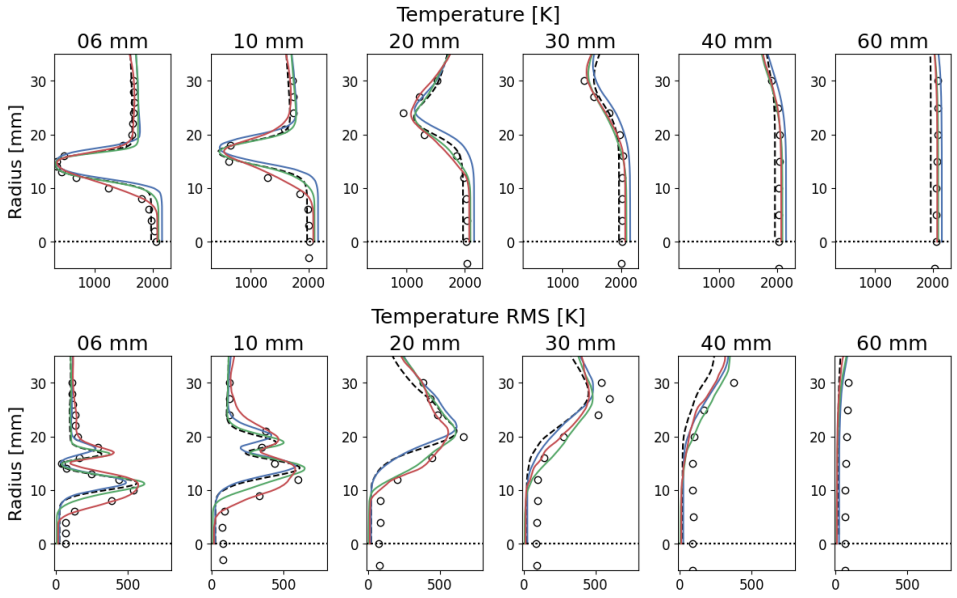

Figure 5: Time averaged and RMS temperature profiles (Flame B): Experiments (o), FGM-14M (- ·), PaSR-4M (—), PaSR-14M (—), PaSR-30M (—).

a shifting of the position of the peaks in comparison. From 20 to 60 mm, a single peak is present for all models, with FGM-14 resulting in a closer match to the experimental data compared to PaSR, evidencing a better prediction of this species in the burned gases region. A clear improvement is seen as mesh resolution is increased for the PaSR at all positions, but especially at 6 and 10 mm. Regarding CO_2, profiles are similar for all models. A very good agreement is found on the reacting layers for PaSR-30M at all positions, while FGM-14 better recovers the mass fraction values in the inner and outer recirculation zones.

As was the case for the flow field, the thermochemical profiles match the experimental data to a satisfying degree for all models, with PaSR-30M showing in general the best temperature and species predictions at the most upstream

positions for the flame front, while FGM-14M provided more consistent results in regions dominated by burned gases, such as the inner and outer recirculation zones. As shown in other studies for non-premixed combustion [20, 21], the PaSR model is capable of recovering the correct flow dynamics and temperature profiles when compared to the experimental cases in this swirl-stabilized premixed flame.

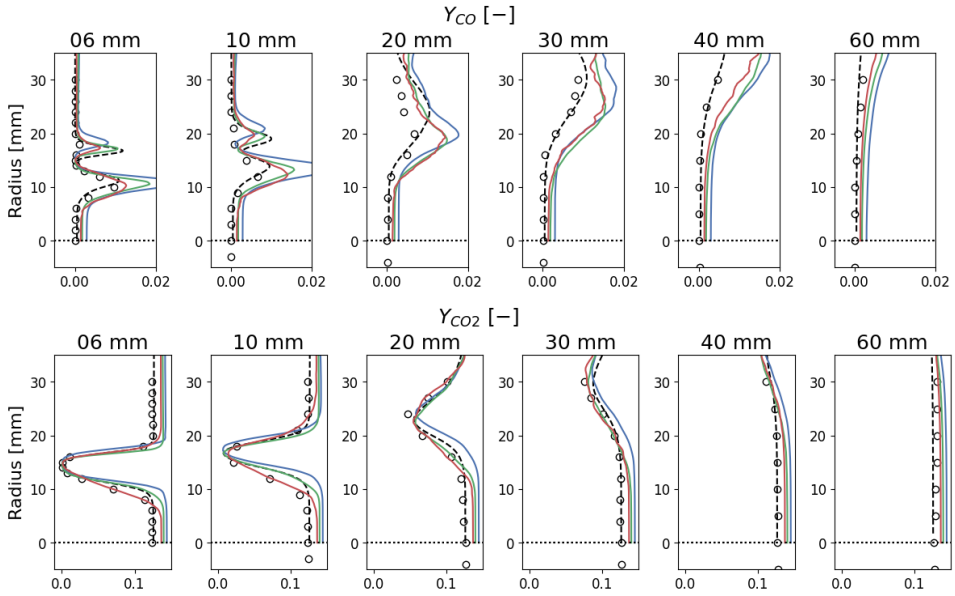

Figure 6: Time averaged profiles for Y_{CO} and Y_{CO_2} (Flame B): Experiments (o), FGM-14M (- ·), PaSR-4M (—), PaSR-14M (—), PaSR-30M (—).

Finally, it is important to note that the simulation times between models and different meshes can vary to a certain degree. Therefore, the time step is not fixed and depends directly on the local flow conditions with a CFL = 0.95. This approach may introduce certain errors when used with operator-splitting if the time-marching uses large-time steps, but as the flow time scales are rather fast due to the turbulent flow, the resolution of the boundary layer with small cells, and the CFL<1, the time steps were below 2.0×10^{-6} s. These values

were suitable for chemical integration with CVODE [42, 44] for this reaction mechanism as part of the stiffness is already removed.

Considering all cases running on the same number of processors of 1472, the required computational expense to achieve a runtime of 10 ms (one pass through flow time) is approximately 4.4 kCPU-hours for FGM on the 14M mesh, while a factor 8 increase is obtained for the PaSR.

4.2. Analysis of the PaSR Quantities

In this section the effects of mesh resolution and heat loss on the PaSR quantities (τ_c, τ_m and κ) are investigated. For such, specific regions of interest in the burner must be chosen and defined. Figure 7 shows time-averaged spatial distributions of axial velocity (left) and temperature (right) for the PaSR-30M case. Iso-contours of axial velocity are also shown on the left side. Of special interest are the the Inner Reacting Layer (IRL), where the sharpest temperature and species gradients occur, and the Outer Reacting Layer (ORL) where smoother gradients occur due to the effect of heat losses. For the longitudinal position of $x = 6$ mm, the IRL is located at $8 < r < 14$ mm, while the ORL is located at $15 < r < 20$. The Inner and Outer Recirculation Zones (IRZ and ORZ) are of limited interest, as the conditions there are close to equilibrium and the reaction rates tend to zero. Also for these regions, chemical time is large ($\kappa \rightarrow 1$) and cells behave as perfectly stirred reactors.

4.2.1. Influence of Mesh Resolution

The PaSR quantities are now compared for the three different meshes (four million, fourteen million and thirty million elements). The overall mesh structure is maintained and only the mesh resolution in the near field of the flame is

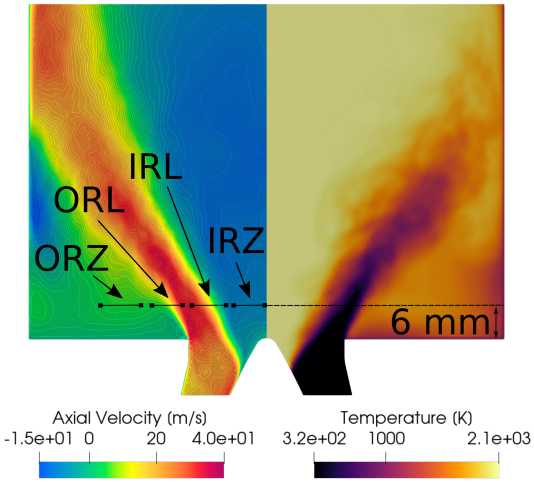

Figure 7: Time-averaged spatial distribution of axial velocity (left) and temperature (right) for the PaSR-30M case (Flame B). The indicated regions, from left to right, correspond to the Outer Recirculation Zone (ORZ), Outer Reacting Layer (ORL), Inner Reacting Layer (IRL) and Inner Recirculation Zone (IRZ).

changed. The flame thickness is used here to express the mesh resolution. In this study, the thermal laminar flame thickness, δ_{th}, is computed from the temperature gradients by:

$$\delta_{th} = \frac{T^b - T^u}{max(\frac{dT}{dx})}, \tag{12}$$

where x represents the spatial component. Considering the $\phi = 0.83$ case, the flame thickness is $\delta_{th} = 0.48$ mm. The length scale on the other hand, is defined as the edge length of the tetrahedral element, $\overline{\Delta}$. Each mesh resolution can be then expressed in terms of the ratio of the thermal flame thickness over its length scale: $\delta_{th}/\overline{\Delta}$, as seen in Table 4. It is expected that as resolution increases, a better description of the flame dynamics and structure can be recovered. Also shown are the correspondent volumes for the cells in the combustion chamber,

which can be calculated as $Vol = \Delta^3$, with $\Delta = \sqrt{(2)}/(12\overline{\Delta}^3)$ for an element in the tetrahedral meshes.

Mesh	Edge length $\overline{\Delta}$ $[mm]$	Mesh resolution $\delta_{th}/\overline{\Delta}$	Vol $[mm^3]$
4M	1.0	0.48	0.118
14M (Baseline)	0.6	0.8	0.025
30M	0.5	0.96	0.015

Table 4: Cell sizes and mesh resolution expressed as the ratio of cell edge length to thermal thickness for each mesh.

The spatial distributions of instantaneous progress variable reaction rate $\dot{\omega}_{Y_c}$ and reacting volume fraction κ on the flame region are presented in Figure 8. For every mesh, the same side is shown and mirrored for the direct comparison of both quantities. Two important points can be illustrated by this figure. First, it is clear to see that with increasing mesh resolution, oscillations and flame wrinkling are better represented, as the size of the elements in the 30M mesh are of the size of the laminar flame thickness. Second, a strong correlation can be seen between the reaction rate of the progress variable and the reacting fraction. This follows directly from Equations 8 and 9, showing that κ has a strong dependence on the chemical time scale, which in turn has a strong dependence on the inverse of $\dot{\omega}_{Y_c}$. It can be noted that for all meshes, when $\dot{\omega}_{Y_c} \to 0$, $\kappa \to 1$. This is valid everywhere except for the fresh gases where the progress variable mass fraction is zero. This region is represented in each mesh by the white iso-contour of the scaled progress variable for a threshold value $C_0 = 0.001$. The strong relationship between κ and $\dot{\omega}_{Y_c}$ (and by extension τ_c) indicate that the influence of τ_m in the reacting fraction is somewhat limited in comparison for the present burner, at least in qualitative terms.

It is interesting then to analyze how both time scales behave, both in physical

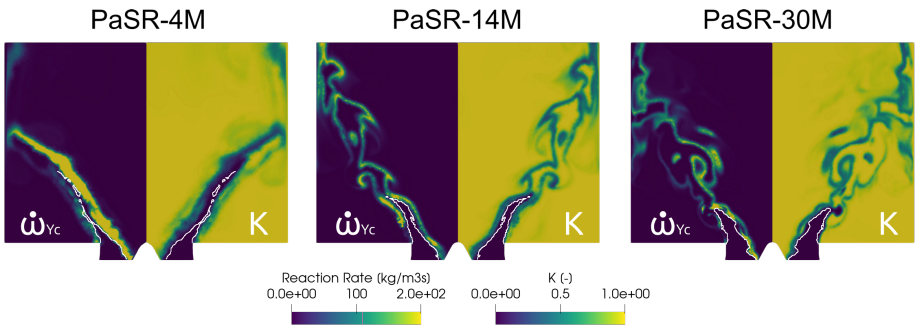

Figure 8: Instantaneous distribution of progress variable reaction rate $\dot{\omega}_{Y_C}$ (left) and reacting volume fraction κ (right) on the flame region. An iso-contour of $C = 0.001$ is also shown to indicate the fresh gases (Flame B).

and composition space. Figure 9 shows the spatial profiles of the time-averaged time scales (left, logarithmic scale) and the volume fraction (right, linear scale) at an axial position of x = 6 mm. The same side is mirrored for consistency and the vertical axis is presented in logarithmic scale for visibility, as the range of chemical time scales varies largely. In contrast, the values of mixing time scale are comparatively constant across the domain, being mostly constrained to the 10^{-4} to 10^{-3} s range. This illustrates that the qualitative aspect of κ is directly linked to the behaviour of the chemical time scale, while its quantitative values depend directly on the local ratios between τ_m and τ_c.

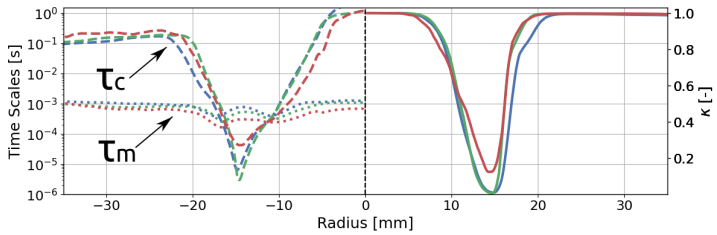

Figure 9: Time averaged profiles of time scales (left) and reacting fraction (right) at 6 mm from the nozzle orifice (Flame B): PaSR-4M (—), PaSR-14M (—), PaSR-30M (—)

Figures 10 and 11 then show the distribution of chemical (violet), mixing (blue) time scales (top row) and the reacting fraction κ (bottom row) for the inner and outer reacting layers, respectively. The plots are shown for the three meshes across the flame front expressed, in terms of normalized temperature, T/T_{eq} where T_{eq} is the equilibrium temperature for each dataset. The dashed lines indicate the conditional average, while the shaded area represent the standard deviation. Considering that the flow through time in this burner is of the order of 10 ms, all cases are run to a minimum of 70 ms and samples are obtained from the final two flow through intervals (20 ms) for each case at an axial position $x = 6$ mm. It is easy to identify that as mesh resolution is increased, the general profile for the mixing time scale remains mostly constant, while at the same time, the profile for the chemical time scale changes considerably. On the preheating zone ($T/T_{eq} < 0.8$), the conditional average for τ_c starts from values smaller than 10^{-6} s in all cases, but remains below the average value of τ_m for PaSR-4M. For PaSR-14M, and crosses the average τ_m at around T/T_{eq} = 0.25. Finally, for PaSR-30M it presents a S shaped profile, with a peak of chemical τ_c close to $T/T_{eq} = 0.4$, from which it drops and decreases again. For all meshes, the chemical time is large as $T \rightarrow T_{eq}$. According to the previous results, chemistry is faster on the coarser mesh at lower temperatures, which in turn drives κ to lower values and reduces the filtered reaction rate globally. As expected, the profiles for the conditional averages of κ follow closely those of τ_c for each mesh. The model is able to provide a value of the reacting fraction that, for each mesh, applies a correction on the filtered reaction rate, such that global reactions are not overestimated. The values of κ are consistently lower for the coarser meshes, implying that for larger elements in the LES domain, a comparatively smaller portion of that element is capable of reacting.

In the outer reacting layer, similarly to the IRL, the conditional average of

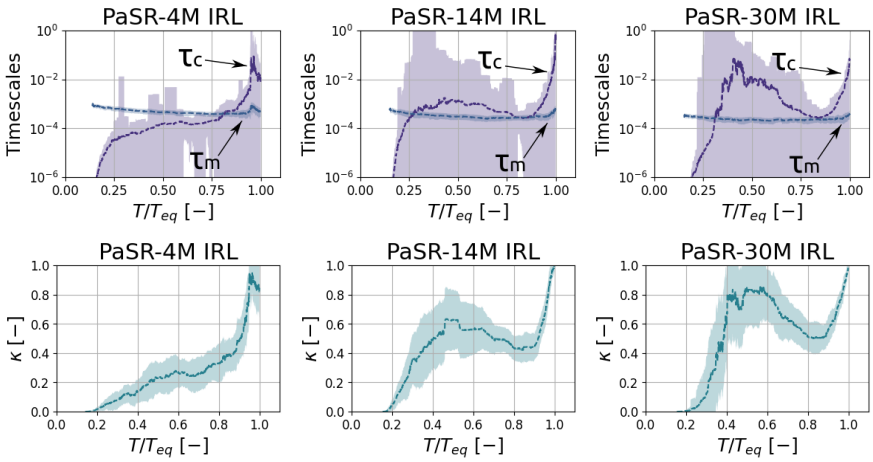

Figure 10: Mean (lines) and standard deviation (shaded areas) of chemical (violet) and mixing (blue) time scales (top row) and volume fraction κ (bottom row) versus normalized temperature in the Inner Reacting Layer (IRL) at at 6 mm from the nozzle orifice (Flame B).

the chemical time scale grows faster in the temperature axis as mesh resolution is increased. On the other hand, chemical times are larger here, compared to the IRL, such that the effect of mesh resolution is lower in this region. This can be attributed to heat loss effect, and will be discussed in the next subsection. As with the chemical time scale, the reacting fraction grows more abruptly as mesh resolution is increased, but the effect is reduced when compared to the IRL.

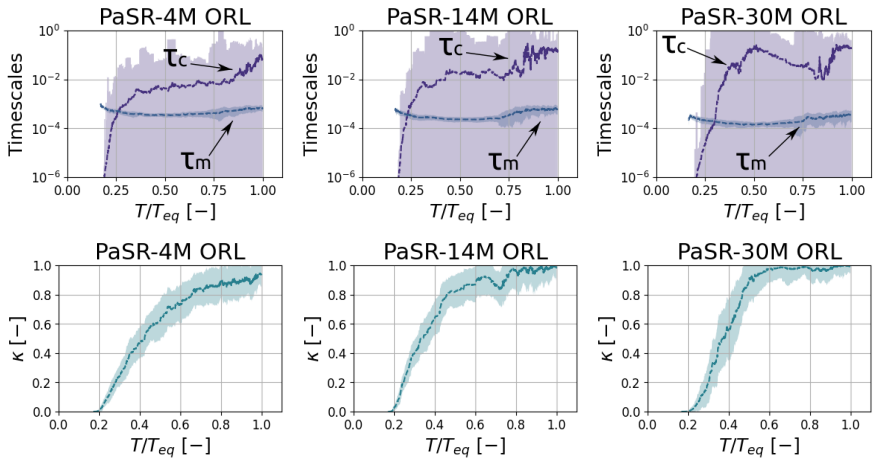

Figure 11: Mean (lines) and standard deviation (shaded areas) of chemical (violet) and mixing (blue) time scales (top row) and volume fraction κ (bottom row) versus normalized temperature in the Outer Reacting Layer (ORL) at 6 mm from the nozzle orifice (Flame B).

4.2.2. Influence of Heat Loss

The effect of heat loss is here analysed for the finest mesh. The influence of heat loss can be seen in 12 in terms of enthalpy and temperature fields by comparing the adiabatic and non-adiabatic solutions. The constant enthalpy distribution confirms the adiabatic assumption, while for the non-adiabatic case, enthalpy is considerably lower on the outer region of the burner due to heat loss to the wall. Additionally, recirculation effects drive burned gases from the outer region towards the inner recirculation zone, lowering enthalpy levels in the IRZ to some degree. For the temperature field, heat loss decreases temperatures, especially in the ORZ. According to that, smoother temperature gradients are found in the outer reacting layer, compared to the adiabatic case (and to the inner reacting layer for both conditions), which reduces the reactivity of the mixture.

Following the enthalpy distribution, temperature is also reduced in the inner regions compared to the adiabatic case. It results that maximum temperature is 100 K higher for the adiabatic condition ($T_{max}^{ad} = 2180$ K, $T_{max}^{non-ad} = 2079$ K).

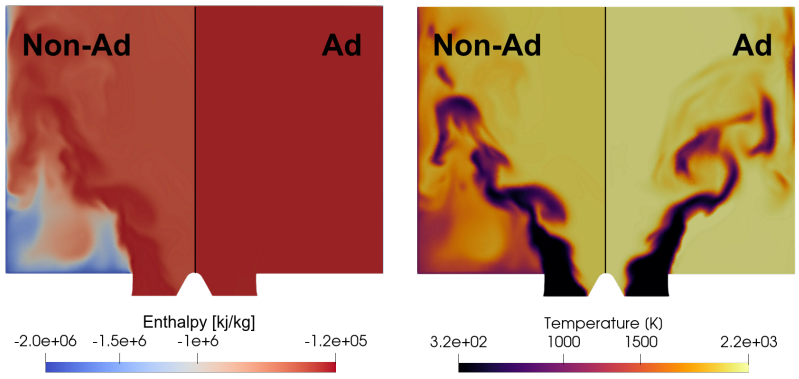

Figure 12: Instantaneous spatial distribution of temperature (left) and enthalpy (right) for non-adiabatic and adiabatic conditions (Flame B).

The time averaged spatial profiles of time scales and reacting fraction between non-adiabatic and adiabatic conditions at $x = 6$ mm are shown in Figure 14. Chemical times are lower for the adiabatic case in the ORL, confirming that chemistry is faster in this region compared to the non-adiabatic condition. In general, the non-adiabatic condition results in slightly faster mixing across the spatial range. Finally, the reacting fraction for the adiabatic case is one order of magnitude lower at its lowest point, compared to the non-adiabatic case, which mimics the behaviour of the chemical time scales.

The reacting fraction for both non-adiabatic (left) and adiabatic (right) conditions are shown in Figure 14 for the IRL (top) and ORL (bottom). In the inner layer, both distributions of κ are similar, with the conditional mean of the adiabatic case showing higher local maximum and lower minimum values in the intermediate temperature range, which can be attributed to the higher

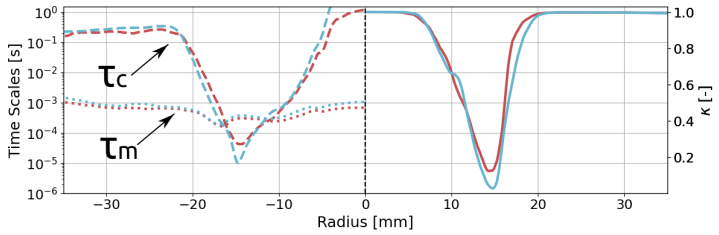

Figure 13: Time averaged profiles of time scales (left) and reacting fraction (right) for non-adiabatic (—) and adiabatic (—) conditions at 6 mm from the nozzle orifice (Flame B).

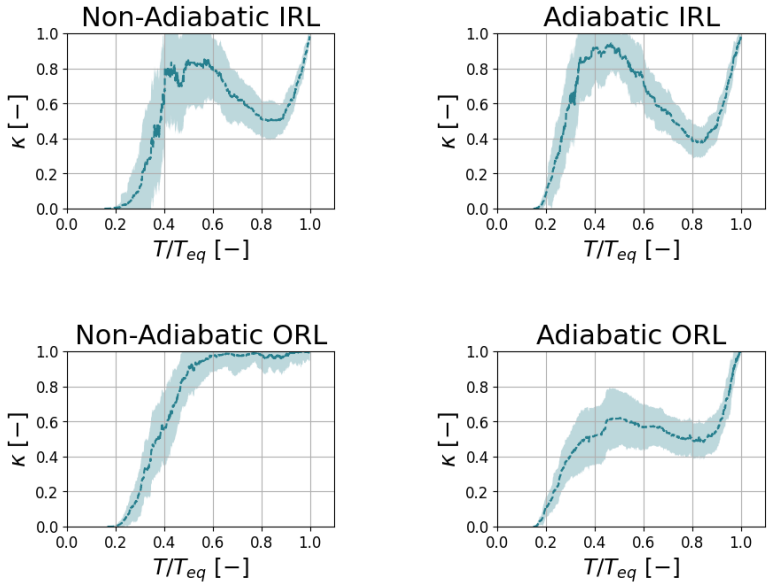

Figure 14: Reacting volume fraction κ versus normalized temperature in the Inner Reacting Layer (top) and Outer Reacting Layer (bottom) at 6 mm from the nozzle orifice (Flame B).

maximum temperature and sharper gradients for this condition. On the ORL side, the qualitative profile of the adiabatic reacting fraction resembles the profiles for the IRL, with a strong S shaped curve, compared to the rapidly growing

behaviour of the non-adiabatic outer layer condition. This is also consistent with the temperature distributions shown in Figure 12. It also shows that the inclusion of heat loss for the non-adiabatic case results in larger reacting fractions at low and intermediate temperature ranges, reaching values close to unity (perfectly stirred regime) around $T/T_{eq} = 0.6$, and remaining in that regime until equilibrium temperatures are reached. In the adiabatic case, the reacting fraction oscillates at intermediate values until rising rapidly to unity as the flame reaches equilibrium ($T/T_{eq} > 0.9$).

4.3. Analysis of the flame structure

The flame structure is now compared between PaSR and experimental data. Figure 15 shows the distribution of the mass fraction of CO in the IRL for the three PaSR meshes, as well as for the experiments. All cases present the expected inverted V profile with CO being produced at intermediate temperatures and eventually consumed when it is converted into CO_2 as equilibrium approaches. When the mesh resolution is increased, a closer correlation with the experimental distribution is achieved, with a similar mean peak value near 0.025 for PaSR-30M. All PaSR profiles however have their distributions shifted towards high temperature regions compared to the experiments, which can be a result of the perfectly premixed assumption. It can also be seen that for PaSR-4M, the levels of CO drop down and start to increase again close to the maximum temperature region. This behaviour is absent for finer meshes and could be an indicator that this mesh resolution is insufficient for capturing the correct flame structure.

Figure 16 shows the distributions of CO_2 for the same region. The conditional mean is similar for all PaSR cases. The experimental case, on the other hand, shows a more abrupt increase in CO_2 levels for lower temperatures, followed by

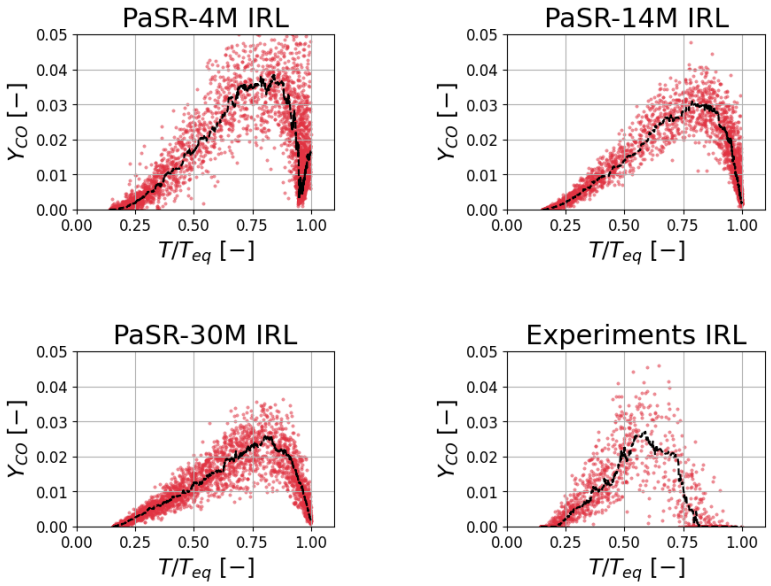

Figure 15: Scatter plots of CO mass fraction versus normalized temperature for the Inner Reacting Layer (IRL) at 6 mm from the nozzle orifice for PaSR and Experimental data. The dashed lines indicates the conditional averages (Flame B).

an inflection point at around 0.7 T/T_{eq}, to finally stabilize at a value close to 0.13. An inflection does occur for PaSR-4M close to high temperature regions but this case also shows the most over-predicted values across all temperature ranges. Once again, the use of the perfectly premixed hypothesis seems to play a role for the numerical cases, resulting in insufficient molecular transport of CO towards low temperature regions.

For the ORL, CO scatter plots can be seen in Figure 17. The conditional averages show a decrease in CO levels for the high temperature regions going from PaSR-4M to PaSR-14M, and a more significant decrease across all temperatures when going to PaSR-30M. Results are still overestimated globally compared to experimental data, where very low levels of CO were captured in this region

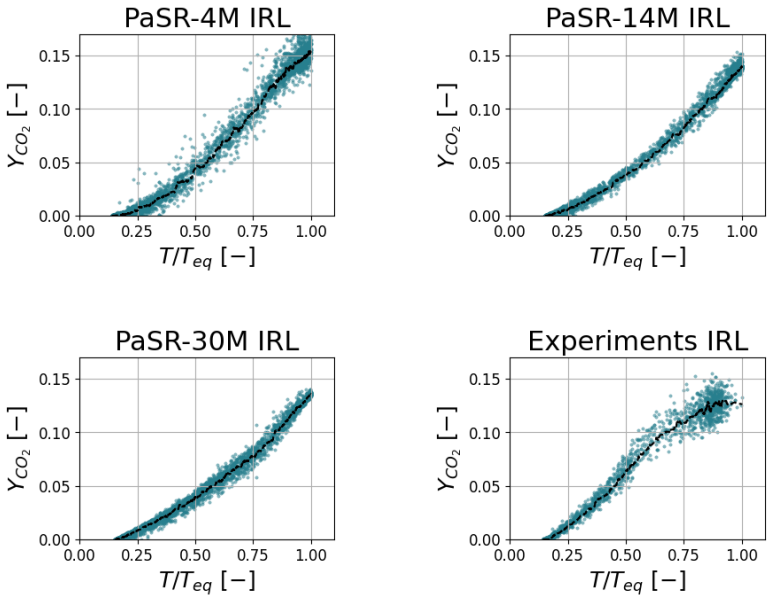

Figure 16: Scatter plots of CO_2 mass fraction versus normalized temperature for the Inner Reacting Layer (IRL) at 6 mm from the nozzle orifice for PaSR and Experimental data. The dashed lines indicates the conditional averages (Flame B).

across all temperatures. The distributions for CO_2 are more consistent with the experiments, with all cases being able to capture the correct distribution and conditional average over the temperature range, even though numerical results still overestimate the CO_2 levels, especially at equilibrium.

Previous stochastic analysis of the PaSR on non-dimensional reactors [45, 19] has shown that a large mixing time is related to a decrease in temperature and production of species. When applied to LES however, it can be seen that the coarser cases, with larger mixing times, resulted in larger overpredictions of both temperature and species. This can be partly attributed to the direct effects of mesh resolution, but also on the relationship between τ_c and τ_m, as for the present work, the chemical time scale has shown to be the most important

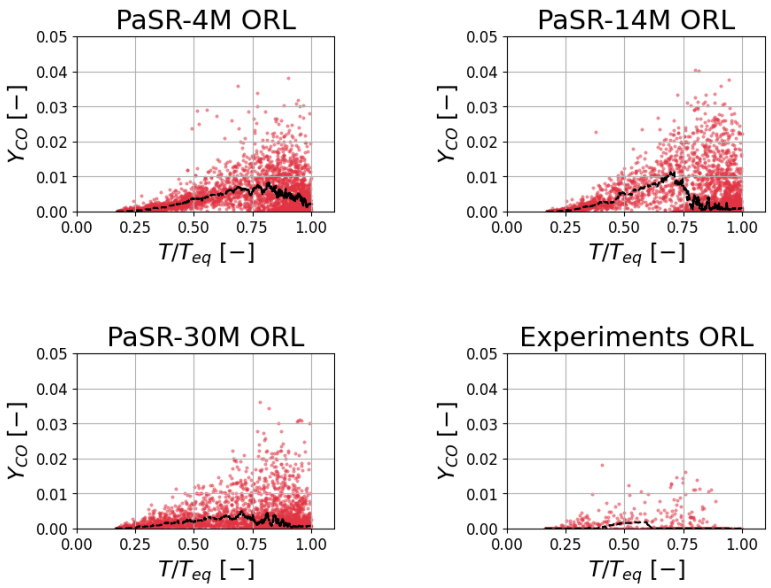

Figure 17: Scatter plots of CO mass fraction versus normalized temperature for the Outer Reacting Layer (ORL) at 6 mm from the nozzle orifice for PaSR and Experimental data. The dashed lines indicates the conditional averages (Flame B).

parameter of the two for computing the reacting fraction, though it shows high sensitivity to mesh resolution.

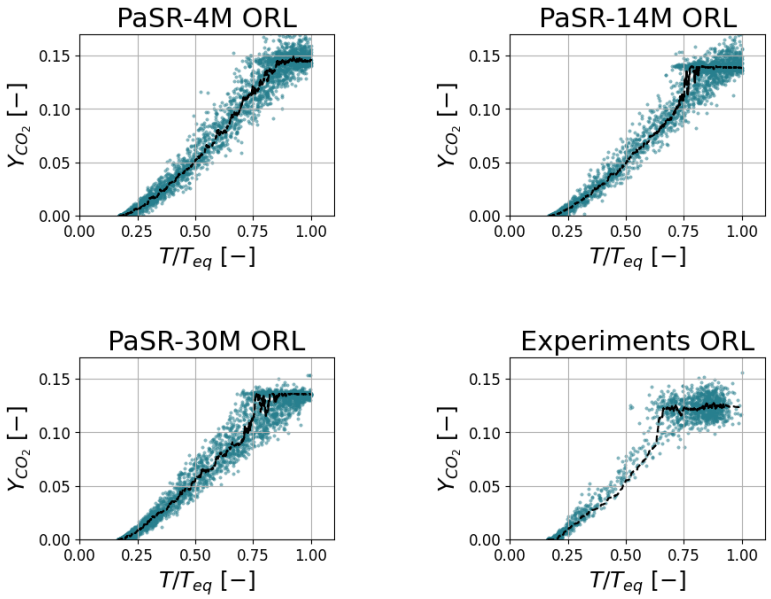

Figure 18: Scatter plots of CO2 mass fraction versus normalized temperature for the Outer Reacting Layer (ORL) at 6 mm from the nozzle orifice for PaSR and Experimental data. The dashed lines indicates the conditional averages (Flame B).

Flame structure can be analyzed in a similar way to asses the role of heat losses. The distributions of the mass fractions of CO and CO_2 are shown in Figures 19 and 20 respectively, for both IRL (top) and ORL (bottom). For both species, profiles are similar in the IRL between non-adiabatic and adiabatic cases. On the ORL on the other hand, the adiabatic profiles present the same general behaviour as their IRL counterpart. The maximum values for both species are also found in the adiabatic ORL, which might indicate faster chemistry in this region. In particular a plateau of the conditional average of CO_2 mass fraction in the ORZ can be only observed for the non-adiabatic case, and more closely resembles the experimental distribution of Figure 18.

Finally, the influence of heat loss can also be evaluated by an analysis of

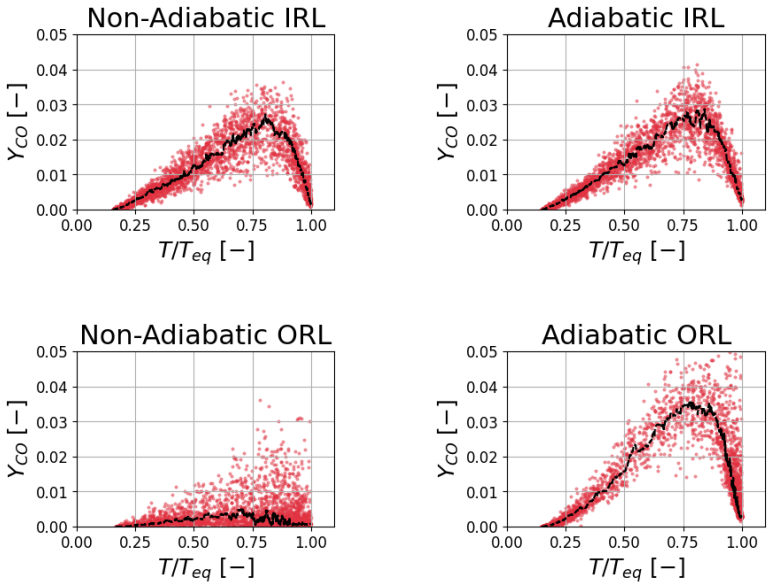

Figure 19: Scatter plots of CO mass fraction versus normalized temperature for the Inner Reacting Layer (top) and Outer Reacting Layer (bottom) at 6 mm from the nozzle orifice for the PaSR at non-adiabatic (left) and adiabatic (right) conditions (Flame B).

the time-averaged distribution of OH. This is shown in Figure 21 for the DLR experiments, non-adiabatic and adiabatic cases, respectively. The experiment is only of qualitative nature, and thus the color scheme is meant to provide a general representation of the flame structure. The inclusion of heat loss mitigates the production of the OH radicals in he outer layer, lowering global levels of the species. Such effect can be seen when comparing both numerical cases to the experimental data. This is particularly evident in the outer recirculation zone, where the adiabatic case results in much higher concentrations of OH, which is consistent with the faster chemistry observed in the earlier discussion. Moving towards the reacting layer, the adiabatic case also overpredicts the OH levels excessively in the outer reacting layer and to a lesser degree in the inner reacting

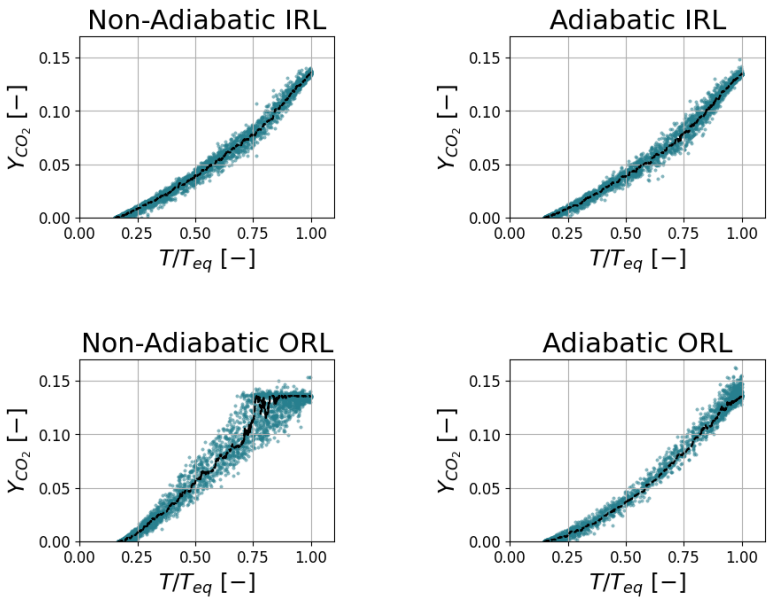

Figure 20: Scatter plots of CO_2 mass fraction versus normalized temperature for the Inner Reacting Layer (top) and Outer Reacting Layer (bottom) at 6 mm for the PaSR at non-adiabatic (left) and adiabatic (right) conditions (Flame B).

layer. Lastly, the inner recirculation zone for the adiabatic case also presents much higher levels of the species compared to the other cases. These results show that the proper modeling of heat loss is fundamental to correctly capture the flame structure and the PaSR has been successful in predicting this effect, both qualitatively and quantitatively.

5. Conclusions

The Partially Stirred Reactor model was applied to an LES of the PRECCINSTA burner. The non-adiabatic simulations were carried out for two distinct equivalence ratios and perfectly premixed conditions. As a first step, three different meshes were used, with distinct mesh resolutions, to asses the influence of mesh

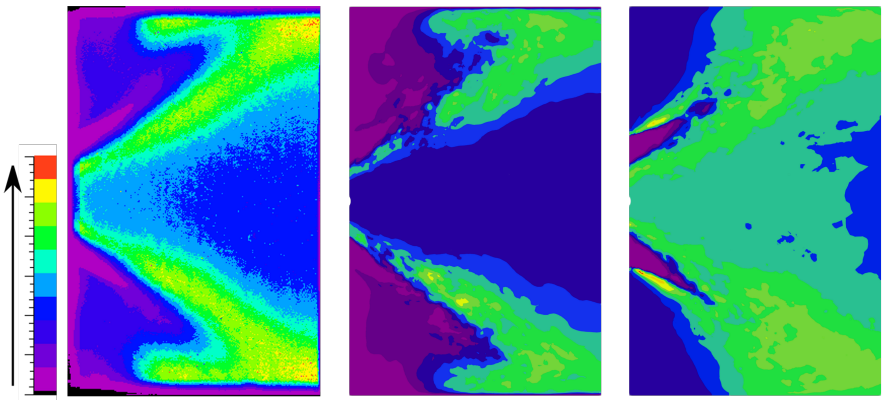

Figure 21: Comparison of time-averaged OH-LIF fields (left) with the OH mass concentrations for non-adiabatic (middle) and adiabatic (right) PaSR simulations on the 30 million elements mesh (Flame B).

resolution on the predictive capabilities of the model. Later on, the adiabatic case was simulated for the finest mesh. The definition of the mixing time scale for the PaSR is based on the dissipation rate of the turbulent kinetic energy in the subgrid scale, while the chemical time scale is based on the definition of the time scale of a progress variable. Results were compared to the tabulated FGM method, using the same definition of the progress variable, as well as to the experimental data.

A very good agreement was found between PaSR to the experimental data considering the time averaged comparison of the flow fields for the $\phi = 0.75$ flame. Only minor deviations in specific regions of the burner were found. Overall, the PaSR was shown to be equivalent to the FGM at predicting flow dynamics. For the $\phi = 0.83$ flame, the time averaged comparison of the thermochemical quantities once again resulted in a good correlation with the experimental data. The best results for the temperature distribution were obtained by the PaSR on the more refined mesh (30 million elements) while FGM performed slightly

better than PaSR for the same reference mesh (14 million). Differences between PaSR and FGM models were minor. The improvement of mesh resolution was shown to result in increasingly better results for the PaSR model.

Considering the influence of mesh resolution on the PaSR quantities, a limited effect is found for the mixing time scale. On the other hand, the chemical time scale is strongly affected by mesh resolution, which in turn directly affects the reacting fraction. This results in a larger reacting fraction for the coarser mesh with an overprediction of the filtered reaction rate. In a similar manner, the effect of heat loss on the PaSR was shown to manifest in two main manners: firstly, it decreases global maximum temperature, which affects the distribution of reacting fraction in the inner reacting layer to a limited degree compared to the adiabatic case. Secondly, it changes the distribution of reacting fractions in the outer shear layer, resulting in higher values at low and intermediate temperatures, reaching the perfectly stirred regime faster compared to the adiabatic case.

Regarding flame structure, mesh resolution was shown to have a key role, with the coarser mesh resulting in elevated temperatures and an overprediction of the levels of CO, especially at high temperatures. All PaSR cases were shown to overpredict the experimental data in the central recirculation to a certain degree, but the improvement in mesh resolution also improves the distributions of species, resulting in a better recovery of the experimental profiles. Heat losses were also shown to be fundamental for the correct prediction of the distributions of CO and CO_2 in the outer reactive layer, where its effects are more evident. As expected, it had a more limited effect in the inner reacting layer. For the OH fields, heat losses were also shown to be essential, making it possible to closely recover the experimental case. The adiabatic case in comparison overpredicts the levels of OH globally.

This work has shown that the PaSR has been successful to predict the dis-

tinctive characteristics of a swirling premixed flame subjected to heat loss. This makes this model a promising closure for LES to address more challenging conditions in non-premixed and partially premixed flames where flamelet methods can have some difficulties and the manifold space can get rather complex and not well-defined.

5. Acknowledgments

This project has received funding from the Center of Excellence in Combustion project (grant agreement No 952181), along with the AHEAD PID2020-118387RB-C31 (CMT) / PID2020-118387RB-C33 (BSC) and ORION PDC2021-121066-C22 (CMT) / PDC2021-121066-C21 (BSC), and H2AERO CPP2022-009921 (BSC) projects from the Ministerio de Ciencia e Innovación. DM acknowledges the grant Ayudas para contratos Ramón y Cajal (RYC 2021): RYC2021-034654-I from Ministerio de Ciencia e Innovación.

5. References

[1] D. Mira, E. J. Pérez-Sánchez, R. Borrell, G. Houzeaux, Hpc-enabling technologies for high-fidelity combustion simulations, Proceedings of the Combustion Institute 39 (4) (2023) 5091–5125. doi:https://doi.org/10.1016/j.proci.2022.07.222.
URL https://www.sciencedirect.com/science/article/pii/S1540748922002516

[2] O. Gicquel, N. Darabiha, D. Thevenin, Laminar premixed hydrogen/air counterflow flame simulations using flame prolongation of ILDM with differential diffusion[Accessed 27-02-2024] (2000).

[3] J. Van Oijen, L. De Goey, Modelling of premixed laminar flames using flamelet-generated manifolds, Combustion Science and Technology 161 (1) (2000) 113–137. arXiv:https://doi.org/10.1080/00102200008935814, doi:10.1080/00102200008935814.
URL https://doi.org/10.1080/00102200008935814

[4] O. Colin, F. Ducros, D. Veynante, T. Poinsot, A thickened flame model for large eddy simulations of turbulent premixed combustion, Physics of Fluids 12 (7) (2000) 1843–1863.

[5] I. S. Ertesvåg, B. F. Magnussen, The eddy dissipation turbulence energy cascade model, Combustion Science and Technology 159 (1) (2000) 213–235.

[6] A. R. Kerstein, A linear- eddy model of turbulent scalar transport and mixing, Combustion Science and Technology 60 (4-6) (1988) 391–421.

[7] A. Klimenko, R. Bilger, Conditional moment closure for turbulent combustion, Progress in Energy and Combustion Science 25 (6) (1999) 595–687.

[8] L. A. Vulis, Thermal Regimes of Combustion, McGraw-Hill Book Company Inc, 1961.

[9] J. Chomiak, A. Karlsson, Flame liftoff in diesel sprays, Symposium (International) on Combustion 26 (2) (1996) 2557–2564.

[10] E. Baudoin, R. Yu, Bai, K. J. Nogenmur, X.-S. Bai, C. Fureby, Comparison of LES models applied to a bluff body stabilized flame, in: 47th AIAA Aerospace Sciences Meeting including The New Horizons Forum and Aerospace Exposition, American Institute of Aeronautics and Astronautics, 2009.

[11] H. G. Im, T. S. Lund, J. H. Ferziger, Large eddy simulation of turbulent front propagation with dynamic subgrid models, Physics of Fluids 9 (12) (1997) 3826–3833.

[12] V. Sabelnikov, C. Fureby, Les combustion modeling for high re flames using a multi-phase analogy, Combustion and Flame 160 (1) (2013) 83–96.

[13] S. Iavarone, M. Cafiero, M. Ferrarotti, F. Contino, A. Parente, A multiscale combustion model formulation for nox predictions in hydrogen enriched jet flames, International Journal of Hydrogen Energy 44 (41) (2019) 23436–23457.

[14] A. Péquin, S. Iavarone, R. M. Galassi, A. Parente, The partially stirred reactor model for combustion closure in large eddy simulations: Physical principles, sub-models for the cell reacting fraction, and open challenges, Physics of Fluids 34 (5) (2022) 055122.

[15] E. Quadarella, A. Péquin, A. Stagni, A. Parente, T. Faravelli, H. G. Im, A generalized partially stirred reactor model for turbulent closure, Proceedings of the Combustion Institute 39 (4) (2023) 5329–5338.

[16] J. R. Edwards, C. Rajath, A. V. Navratil, Multi-resolution analysis of partially-stirred reactor models for subgrid turbulence/chemistry interactions, Computers & Fluids 275 (2024) 106235.

[17] C. Fureby, Large eddy simulation modelling of combustion for propulsion applications, Philosophical Transactions of the Royal Society A: Mathematical, Physical and Engineering Sciences 367 (1899) (2009) 2957–2969.

[18] E. Giacomazzi, C. Bruno, B. Favini, Fractal modelling of turbulent combustion, Combustion Theory and Modelling 4 (4) (2000) 391.

[19] C. Yu, L. Cai, J.-Y. Chen, Stochastic modeling of partially stirred reactor (pasr) for the investigation of the turbulence-chemistry interaction for the ammonia-air combustion, Flow, Turbulence and Combustion (2023) 1–28.

[20] X. Qian, C. Zou, H. Lu, H. Yao, Large-eddy simulation of cambridge-sandia stratified flames under high swirl, Combustion and Flame 244 (2022) 112241.

[21] R. Palulli, S. Dybe, K. Zhang, F. Güthe, P. R. Alemela, C. O. Paschereit, C. Duwig, Characterisation of non-premixed, swirl-stabilised, wet hydrogen/air flame using large eddy simulation, Fuel 350 (2023) 128710.

[22] A. Piscopo, W. de Paepe, A. Parente, S. Iavarone, Chemical timescale analysis of the partially stirred reactor model in a hydrogen-fuelled scramjet, Results in Engineering (2024) 102834.

[23] W. Meier, P. Weigand, X. Duan, R. Giezendanner-Thoben, Detailed characterization of the dynamics of thermoacoustic pulsations in a lean premixed swirl flame, Combustion and Flame 150 (1) (2007) 2–26. doi:https://doi.org/10.1016/j.combustflame.2007.04.002.
URL https://www.sciencedirect.com/science/article/pii/S0010218007000855

[24] S. Roux, G. Lartigue, T. Poinsot, U. Meier, C. Bérat, Studies of mean and unsteady flow in a swirled combustor using experiments, acoustic analysis, and large eddy simulations, Combustion and Flame 141 (1-2) (2005) 40–54.

[25] J. Galpin, A. Naudin, L. Vervisch, C. Angelberger, O. Colin, P. Domingo, Large-eddy simulation of a fuel-lean premixed turbu-

lent swirl-burner, Combustion and Flame 155 (1) (2008) 247–266. doi:https://doi.org/10.1016/j.combustflame.2008.04.004.
URL https://www.sciencedirect.com/science/article/pii/S0010218008000990

[26] B. Fiorina, R. Vicquelin, P. Auzillon, N. Darabiha, O. Gicquel, D. Veynante, A filtered tabulated chemistry model for LES of premixed combustion, Combustion and Flame 157 (3) (2010) 465–475.

[27] P. Wang, N. Platova, J. Fröhlich, U. Maas, Large eddy simulation of the preccinsta burner, International Journal of Heat and Mass Transfer 70 (2014) 486–495.

[28] P. Wang, J. Fröhlich, U. Maas, Z.-x. He, C.-j. Wang, A detailed comparison of two sub-grid scale combustion models via large eddy simulation of the preccinsta gas turbine model combustor, Combustion and Flame 164 (2016) 329–345.

[29] B. Franzelli, E. Riber, L. Y. Gicquel, T. Poinsot, Large eddy simulation of combustion instabilities in a lean partially premixed swirled flame, Combustion and flame 159 (2) (2012) 621–637.

[30] S. Gövert, D. Mira, J. B. W. Kok, M. Vázquez, G. Houzeaux, The effect of partial premixing and heat loss on the reacting flow field prediction of a swirl stabilized gas turbine model combustor, Flow, Turbulence and Combustion 100 (2) (2017) 503–534. doi:10.1007/s10494-017-9848-4.
URL https://doi.org/10.1007%2Fs10494-017-9848-4

[31] D. Mira Martinez, X. Jiang, C. Moulinec, D. Emerson, Numerical assessment of subgrid scale models for scalar transport

in large-eddy simulations of hydrogen-enriched fuels, International Journal of Hydrogen Energy 39 (14) (2014) 7173–7189. doi:https://doi.org/10.1016/j.ijhydene.2014.03.018.
URL https://www.sciencedirect.com/science/article/pii/S0360319914006314

[32] S. Gövert, D. Mira, J. Kok, M. Vázquez, G. Houzeaux, Turbulent combustion modelling of a confined premixed jet flame including heat loss effects using tabulated chemistry, Applied Energy 156 (2015) 804–815. doi:https://doi.org/10.1016/j.apenergy.2015.06.031.
URL https://www.sciencedirect.com/science/article/pii/S0306261915007898

[33] R. S. Freitas, A. Péquin, R. M. Galassi, A. Attili, A. Parente, Model identification in reactor-based combustion closures using sparse symbolic regression, Combustion and Flame 255 (2023) 112925. doi:https://doi.org/10.1016/j.combustflame.2023.112925.
URL https://www.sciencedirect.com/science/article/pii/S0010218023003061

[34] D. Mira, O. Lehmkuhl, A. Both, P. Stathopoulos, T. Tanneberger, T. G. Reichel, C. O. Paschereit, M. Vázquez, G. Houzeaux, Numerical characterization of a premixed hydrogen flame under conditions close to flashback, Flow, Turbulence and Combustion 104 (2020) 479–507.

[35] B. Franzelli, E. Riber, B. Cuenot, Impact of the chemical description on a large eddy simulation of a lean partially premixed swirled flame, Comptes Rendus Mécanique 341 (1-2) (2013) 247–256.

[36] M. Vásquez, G. Houzeaux, S. Koric, A. Artigues, J. Aguado-Sierra, R. Arís,

D. Mira, H. Calmet, F. Cucchietti, H. Owen, A. Taha, , J. M. Cella", Alya: Towards exascale for engineering simulation codes (2014).

[37] A. Both, O. Lehmkuhl, D. Mira, M. Ortega, Low-dissipation finite element strategy for low mach number reacting flows, Computers & Fluids 200 (2020) 104436.

[38] F. Banchelli, G. Oyarzun, M. Garcia-Gasulla, F. Mantovani, A. Both, G. Houzeaux, D. Mira, A portable coding strategy to exploit vectorization on combustion simulations, Computers Fluids 271 (2024) 106151. doi:https://doi.org/10.1016/j.compfluid.2023.106151.
URL https://www.sciencedirect.com/science/article/pii/S0045793023003766

[39] A. W. Vreman, An eddy-viscosity subgrid-scale model for turbulent shear flow: Algebraic theory and applications, Physics of Fluids 16 (10) (2004) 3670–3681. doi:10.1063/1.1785131.
URL https://doi.org/10.1063%2F1.1785131

[40] S. D. Cohen, A. C. Hindmarsh, P. F. Dubois, et al., CVODE, a stiff/nonstiff ODE solver in C, Computers in physics 10 (2) (1996) 138–143.

[41] Z. Lu, H. Zhou, S. Li, Z. Ren, T. Lu, C. K. Law, Analysis of operator splitting errors for near-limit flame simulations, Journal of Computational Physics 335 (2017) 578–591. doi:https://doi.org/10.1016/j.jcp.2017.01.044.
URL https://www.sciencedirect.com/science/article/pii/S0021999117300608

[42] A. Surapaneni, D. Mira, Assessment of dynamic adaptive chemistry with

tabulated reactions for the simulation of unsteady multiregime combustion phenomena, Combustion and Flame 251 (2023) 112715.

[43] S. Luca, A. N. Al-Khateeb, A. Attili, F. Bisetti, Comprehensive validation of skeletal mechanism for turbulent premixed methane–air flame simulations, Journal of Propulsion and Power 34 (1) (2018) 153–160. doi:10.2514/1.b36528.
URL https://doi.org/10.2514%2F1.b36528

[44] G. Ramirez-Miranda, D. Mira, E. J. Pérez-Sánchez, A. Surapaneni, R. Borrell, G. Houzeaux, M. Garcia-Gasulla, Dynamic load balance of chemical source term evaluation in high-fidelity combustion simulations, Computers Fluids 250 (2023) 105723. doi:https://doi.org/10.1016/j.compfluid.2022.105723.
URL https://www.sciencedirect.com/science/article/pii/S0045793022003164

[45] S. Cannon, B. Brewster, L. Smoot, Stochastic modeling of co and no in premixed methane combustion, Combustion and Flame 113 (1-2) (1998) 135–146.